Interfacial solar vapor generation for desalination and brine treatment: Evaluating current strategies of solving scaling

Linlin Zang[a,b], Casey Finnerty[b], Sunxiang Zheng[b], Kelly Conway[b], Liguo Sun[c], Jun Ma[a,*], Baoxia Mi[b,*]

[a] State Key Laboratory of Urban Water Resource and Environment, School of Environment, Harbin Institute of Technology, Harbin 150090, China
[b] Department of Civil and Environmental Engineering, University of California, Berkeley, California 94720, United States
[c] School of Chemical Engineering and Materials, Heilongjiang University, Harbin 150080, China

Keywords:
Interfacial evaporation
Solar energy
Desalination
Salt resistance
Energy efficiency

a b s t r a c t

Interfacial solar vapor generation, an efficient, sustainable, and low-cost method for producing clean water, has attracted great interest for application in solar desalination and wastewater treatment. Although recent studies indicated significant enhancement of overall performance by developing photothermal materials and constructing different dimensional systems, stable evaporation performance and long-term operation of the evaporator are hindered by severe scaling issues. In this critical review, we present the latest strategies in reducing salt accumulation on the evaporator for solar desalination and brine treatment. We first demonstrate the consequences of salt accumulation, and then discuss various self-cleaning methods based on bio-inspired concepts and other strategies such as physical cleaning, ion rejection and exchange, fast ion diffusion, and controlled crystallization, etc. Importantly, we discuss and address the rational design of the evaporator via establishing a relationship model between its porosity, thickness, and thermal conductivity. Lastly, we evaluate salt-resistance strategies, evaporation performance, and possibilities of real application in different evaporation systems with scaling-resistant abilities.

1. Introduction

The shortage of fresh water remains a severe and challenging issue around the world due to population growth, climate change, and industrial pollution. According to a recent report released by World Research Institute (WIR), about a quarter of the world's population faces an "extreme water shortage" crisis. To alleviate this water scarcity, desalination is expected to become a primary supplier of high-quality water (Tong and Elimelech, 2016). However, reverse osmosis (RO)-based desalination systems require a large amount of energy and cost to maintain the operation of desalination plants, such as pressure recovery infrastructure, pretreatment of influent water, and periodic cleaning of filters. Many underdeveloped regions cannot afford the financial risk of investing in RO, let alone the cost associated with burning fossil fuels to supply the required energy that emit greenhouse gases contributing to air pollution and climate change (Zhang et al., 2019a). Additionally, an RO-based desalination system is unsuitable for treating highly saline wastewater (known as brine) because of the high-pressure requirements associated with operation, as well as a shorten service life resulting from frequent cleanings.

To address the above issues, interfacial solar vapor generation has been proposed to be a sustainable, energy-efficient, and low-cost process in which water vapor generation is accelerated by localized photothermal heating and the resulting water vapor is subsequently collected by condensation. So far, various photothermal materials including carbon materials, semiconductors, and plasmonic metals have been widely used to harvest solar energy to achieve efficient photothermal conversion. Through rationally optimized configurations of evaporators and designing structures of photothermal materials, excellent evaporation performance can be achieved due to stronger light absorption and less heat dissipation. For example, our previous work first presented that an artificial tree configuration effectively enhanced water evaporation through heat localization on the graphene oxide (GO) leaf, leading to a high evaporation rate of 2.0 LMH under 0.82-sun illumination (Mi et al., 2019; Finnerty et al., 2017a). Recently, some studies have shown that the vaporization enthalpy of water from hydrogels and graphene oxide foams could be significantly decreased by increasing hydrophilic groups and controlling the volume of water inflow, respectively (Zhou et al., 2019a; Zhao et al., 2018a; Zhou et al., 2018; Liang et al., 2019; Guo et al., 2019a;

* Corresponding authors.
E-mail addresses: majun@hit.edu.cn (J. Ma), mib@berkeley.edu (B. Mi).

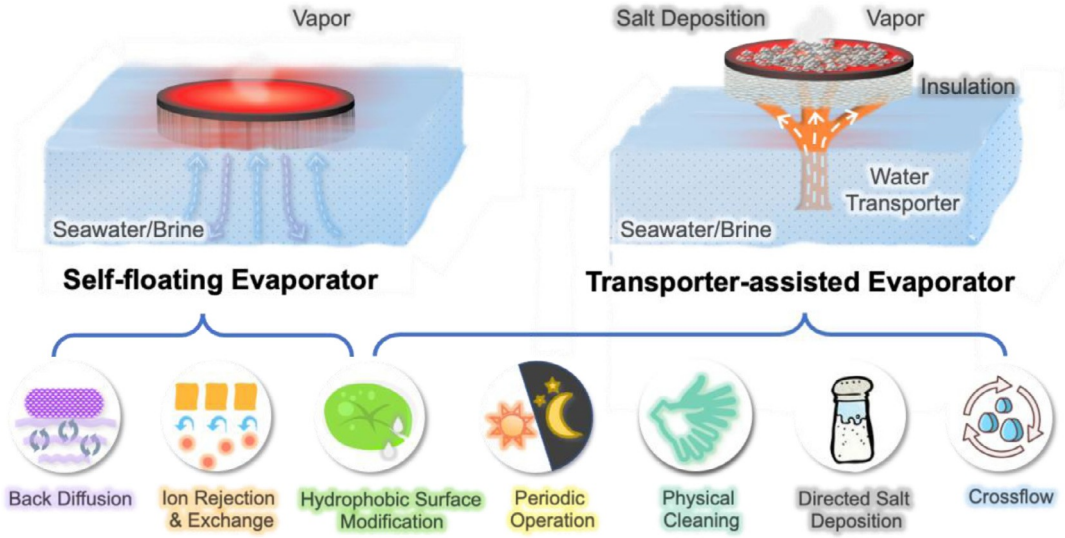

Fig. 1. Current strategies to solve salt scaling on evaporators during the interfacial solar desalination.

Guo et al., 2019b; Guo et al., 2020a). The mechanism basically involves the adjustment of different states of water in a polymer network or porous hydrophilic structure, thereby reducing the heat required for vaporization. As a result, the evaporation rate can exceed 3.0 kg m^{-2} h^{-1} under one-sun illumination, while the light- to-evaporation conversion efficiency approaches 100%. To further improve light utilization, a sunflower-like biomimetic omnidirectional tracker based on nanostructured stimuli-responsive polymers was designed so that the artificial phototropic system can maximize light harvesting under different angles of illumination (Qian et al., 2019).

and three-dimensional (3D) evaporators can still reach 3–8 kg m^{-2} day^{-1} after operating continuously for 6–10 h under natural sunlight (Sun et al., 2020; Fang et al., 2019; Xiao et al., 2019a). Moreover, by using a special wettability housing or electric fans, the condensation process can be greatly accelerated, so as to make full use of the advantages of fast evaporation and improve the overall performance (Chen et al., 2011; Durkaieswaran and Murugavel, 2015; Hou et al., 2015; Wang et al., 2019a).

Undoubtedly, these major breakthroughs have significantly enhanced the performance of photothermal evaporation, enlightening future applications, and laying a solid theoretical foundation. However, in actual seawater with complex compositions and saline water with high concentrations of salts, the evaporation rate and energy conversion efficiency of the evaporator could be seriously affected by various inorganic from the water. In particular, small salt ions (such as Na^+, K^+, $Ca^{2+}$and Mg^{2+}, etc.) are transported from the bulk water to the photothermal materials via capillary action along with the water flow. If the salt ions are unable to diffuse back into the bulk solution, they will gradually concentrate and eventually crystallize at the evaporation sites of the photothermal materials. After a period of time, salt scale can affect light absorption, water supply, vapor diffusion, and even reduce service life and increase equipment operating costs. Obviously, addressing the salt fouling problem is crucial for solar desalination applications. An ideal evaporator for solar desalination needs to meet three conditions: 1) salt crystallization is either prevent or accounted for so that it does not hinder long-term evaporative performance; 2) when preventing scale formation, high salt concentrations do not have much influence on the evaporation rate and solar-to-vapor energy conversion efficiency of the evaporator; 3) the high concentration of salt ions (including monovalent and divalent ions) does not have a significant effect on the structural stability and service life of the evaporator.

So far, the most common evaporation systems are self-floating evaporation configurations and transporter-assisted evaporation configurations. Considering the structural characteristics of each evaporator, different strategies are needed to eliminate salt scale. Herein, our critical review aims to summarize current strategies for reducing salt accumulation on the evaporators (**Fig. 1**) and evaluate them from different perspectives including evaporator design, evaporation performance and applicable scenarios.

2. Evaluation and discussion

2.1. Self-floating evaporators

Wang's group first proposed this novel concept of using self-floating evaporators without any assistance to enhance solar evaporation in 2011 (Zeng et al., 2011). In this report, magnetic Fe_3O_4/C particles floating on the water surface are used as a light-absorbing material to realize the interfacial evaporation process. A small number of light-absorbing materials (115 g m^{-1}) was required to obtain a water evaporation rate of up to 2.3 L m^{-2} h^{-1} at a light intensity of 1355 W m^{-2}, while achieving recyclability and a reduced operating cost. In recent years, due to the advantages of simplified outdoor desalination equipment and reduced operating costs, more and more people have paid attention to the design of self-floating evaporators. Generally, in order to construct a self-floating evaporator, it needs to have a photothermal surface for

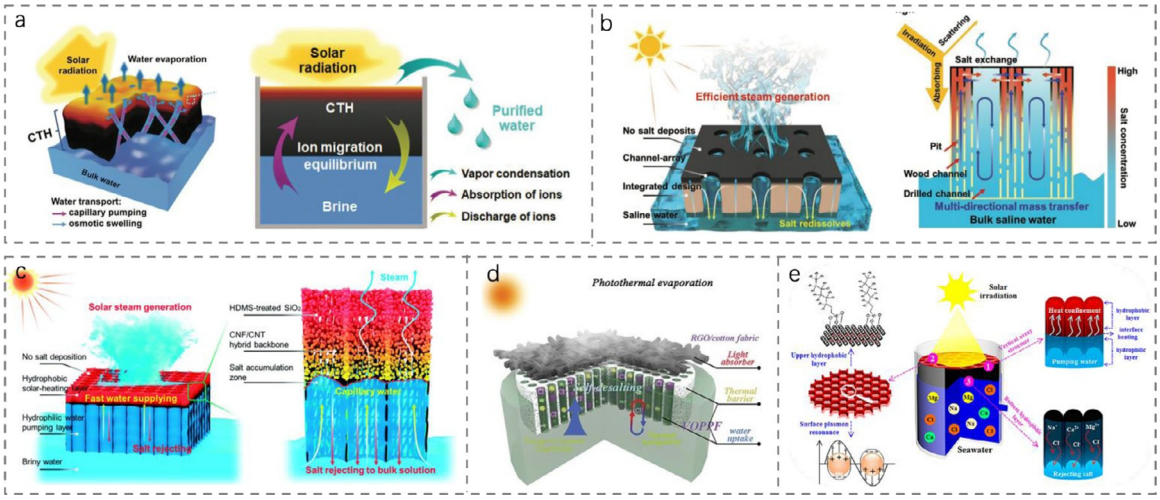

Fig. 2. Salt-resistant self-floating evaporator for solar desalination. a) Schematic illustration of solar desalination based on the rGO/PVA hydrogel-based evaporator (Zhou et al., 2018). Copyright 2018 The Royal Society of Chemistry. b) Natural wood-based evaporator with rationally designed artificial channel-array (Kuang et al., 2019). Copyright 2019 Wiley-VCH. c) Janus evaporator with low tortuosity based on a hydrophobic SiO_2 /cellulose nanofibers/carbon nanotube hybrid network (Hu et al., 2019). Copyright 2019 The Royal Society of Chemistry. d) Self-desalting solar evaporation system comprising reduced graphene oxide/cotton fabric on a vertically oriented porous polyacrylonitrile foam (Zhang et al., 2019b). Copyright 2019, The Royal Society of Chemistry. e) Vertically aligned Janus MXene-based aerogels for solar desalination with high efficiency and salt resistance (Zhang et al., 2019c). Copyright 2019 American Chemistry Society. (For interpretation of the references to colour in this figure legend, the reader is referred to the web version of this article.)

vapor generation, abundant hydrophilic pores for water transport, and excellent thermal insulation for high energy efficiency. During solar desalination, salt ions will be transported along the porous channels to the evaporation surface via capillary action. As a result, an ion concentration gradient is gradually built up between the surface and the bulk solution. Once the ion concentration exceeds the solubility limit, the salt crystals form, covering the evaporation surface and blocking the water-transport channels. Additionally, the thickness of the evaporator has an effect on the transport and diffusion of salt ions as well as heat conduction loss. Therefore, self-floating evaporators need to be rationally designed to avoid salt deposition and minimize energy loss.

2.1.1. *Back diffusion*

conversion applications, and water-related treatment (Wang et al., 2016; Zang et al., 2017; Qi et al., 2017; Puperi et al., 2016). It is well known that hydrogels have a chemically or physically cross-linked polymer network and then form interconnected pores via drying technique, which helps to increase the surface area and accelerate the mass/charge transport inside the structure (Guo et al., 2020b). Due to the abundant hydrophilic groups in the molecular chain (such as -OH, -COOH, $-SO_3H$ and $-NH_2$), they can interact with water molecules through hydrogen bond and electrostatic interaction, resulting in a large amount of water holding in a 3D hierarchical structure (Guo et al., 2020b; Zhou et al., 2019b). Importantly, dehydrated hydrogels are able to generate swelling pressure after absorbing water due to the extension of their polymer chains (Li et al., 2011). For this reason, they have been used as draw agents to extract water through forward osmosis (Hartanto et al., 2016; Zeng et al., 2019a; Razmjou et al., 2013a; Razmjou et al., 2013b; Cai et al., 2013). Recently, Zhou *et al.* introduced reduced graphene oxide (rGO) into a polyvinyl alcohol (PVA) hydrogel to prepare an antifouling solar evaporator (Zhou et al., 2018). It has been well-characterized that within the 3D network of hydrogels, water exists in three states, including free water, intermediate water, and bound water, which can effectively reduce vaporization enthalpy of the water by rationally tailoring water states, thereby achieving high evaporation rates and energy efficiency. In the solar-driven desalination process, the interconnected porous structure of the hydrogel-based evaporator, including internal gaps and microchannels, allows rapid water transport by capillary pumping and osmotic swelling, while salt ions diffuse and migrate into the bulk solution (**Fig. 2a**). As a result, this dynamic equilibrium process between water transport and ion discharge keeps a constant ion concentration in the hydrogel, thereby restricting the ion accumulation and the salt deposition. Even when processing highly concentrated brines (5 wt%−20 wt%), the hydrogel still retains its salt-resistant performance, high evaporation rates (>2.2 kg m^{-2} h^{-1}), and energy conversion efficiencies (>90%). However, as the concentration of salt ions increased, the size of the hydrogel shrunk significantly after 12 h of illumination. Although the hydrogel-based evaporator has great potential in long-term solar desalination, its unstable morphology might limit its further application in treating highly concentrated brines.

It is well known that natural wood possesses good structural stability, excellent hydrophilicity, low thermal conductivity of 0.11~0.33 W m^{-1} K^{-1} in dry state and aligned channels along the growth direction that are capable of transporting water to the leaves by capillary force. Therefore, after the surface of pristine natural wood is carbonized at high temperature or modified by various light absorbers (e.g., carbon nanotubes, GO, polydopamine and plasmonic metal nanoparticles) (Zhu et al., 2017; Zhu et al., 2018; Liu et al., 2018; Liu et al., 2017; Wu et al., 2017; Wang et al., 2019b), it can be directly used as a self-floating photothermal evaporator. However, the surface and water channels of the wood-based evaporator tend to get clogged by the solid salts under concentrated solar illumination or with highly concentrated brines. He et al. found that natural balsa wood has larger vessel channels along the tree growth direction ranging from 18 to 390 μm and a large number of pits of 1–2 μm on the cell wall (He et al., 2019). The hierarchically porous structure is beneficial to replenish sufficient water to the evaporation surface and promote two-directional ion diffusion. The results indicated that the balsa wood-based evaporator with a thickness of 4.5 mm can achieve a stable evaporation rate of 1.7 kg m^{-2} h^{-1} without any salt accumulation when it was in 15 wt% brine and exposed to 2-sun illumination for 20 days (7 h/day). In order to further improve the

evaporator's salt-resistant ability, several millimeter-sized channels were drilled on the surface of the natural wood-based evaporator with a thickness of 20 mm (**Fig. 2b**) (Kuang et al., 2019). Due to the larger hydraulic conductivity compared with the natural micropores, the artificial channels can be used as an effective pathway for ion diffusion. As a result, the evaporator demonstrated continuous operation for over 100 h in 20 wt% NaCl solution under one-sun irradiation, as well as excellent salt resistance ability and energy efficiency (~75%). Although the desalination capacity of the wood-based evaporator has been greatly improved, its solar-to-vapor energy conversion efficiency is still less than 80% under one-sun illumination. By increasing the size of water channels used for the back diffusion of salts, the effective thermal conductivity of their evaporator likely increased as well. This results in a lower solar- to-vapor efficiency because more of the heat being generated by the photothermal material is now being conducted away from the evaporative interface, lowering the available energy for evaporation.

Inspired by the naturally porous structure supplying capillary action, self-floating evaporators with artificially aligned channels have been successfully manufactured by directional growth of ice crystals in polymers (e.g., polyacrylonitrile) or nanomaterials (e.g., Mxene and cellulose nanofibers), followed by freeze drying (**Fig. 2c-2e**). To demonstrate the superiority of the evaporators with low-tortuosity porous structure, Hu et al. compared the salt-resistance and long-term stability with those evaporators with a random porous structure (Hu et al., 2019). They found the former can accelerate the rates of ion diffusion and after 100 h of continuous evaporation in simulated seawater, the evaporation rate was stable at 1.2~1.3 kg m^{-2} h^{-1} without salt deposition. In contrast, the surface of the latter was partially covered by the solid salt and showed a decreasing trend in the evaporation rate. In addition, since the porous evaporator has multiple functions of water transport and ion diffusion as well as the thermal insulation, the thickness is very important for the overall evaporation performance. Therefore, Zhang et al. designed a vertically oriented porous polyacrylonitrile (PAN) foam with a thickness of 25 mm and placed a reduced graphene oxide (rGO)/cotton fabric photothermal material on top (Zhang et al., 2019b). Due to a lower thermal conductivity (0.21 W m^{-1} K^{-1}) in the wet state than pure water (0.6 W m^{-1} K^{-1}), the temperature difference between the evaporation surface and the bulk water can reach around 17°C, thereby resulting in a high evaporation efficiency of about 90%. Meanwhile, no salt accumulation was observed on the rGO/cotton fabric after exposure to one-sun illumination for 12 h in 3.5 wt% NaCl solution. Because the thickness of the as-prepared evaporator can be customized by changing the volume of the casting solution, Zhang et al. presented vertically aligned Janus Mxene-based aerogels with different thicknesses for the solar-driven desalination and found the thicker aerogel is conducive for greater heat localization capacity, but also reduces water transport through the long porous channels and slows the water evaporation rate (Zhang et al., 2019c). Although the biomimetic strategy is quite simple and feasible, the diameter distribution of vertically oriented pores is mainly concentrated in tens of microns (15~40 μm) due to the preparation method. The researchers did not further investigate their long-term salt-resistant performance in high-salinity brines, although the low-tortuosity channels may also demonstrate similar advantages in preventing salt precipitation on the evaporator surface.

In summary, it is necessary to rationally design the self-floating evaporator to simultaneously achieve excellent salt resistance performance and high energy conversion efficiency. As shown in **Fig. 3**, the accumulation of salt on the evaporator has the potential to increase the reflection of incoming light and reduce the energy available for evaporation. Additionally, our previous work demonstrated that salt precipitation impedes evaporation, resulting a higher surface temperature and an increase in other heat loss mechanisms (e.g., radiation, convection, and conduction). To understand the relationship between different parameters of an ideal salt-resistant evaporator (i.e., porosity, tortuosity, and thickness) and solar-to-vapor energy conversion efficiency, we developed a simple ion-transport model to predict how salt accumulation can be eliminated while maintaining a high energy efficiency.

First, we assume the diffusion flux of the salt ion in the porous channels is J_{diff} (kg-salt m^{-2} s^{-1}) which can be calculated using Fick's laws of diffusion:

$$J_{diff} = -D\frac{d\phi}{d_x} = \frac{\varepsilon D(C_s - C_b)}{\tau L} \quad (1)$$

where D is the diffusion coefficient of NaCl in water (1.6×10^{-9} m^2 s^{-1}); C_s and C_b (kg m^{-3}) are the ion concentrations at the photothermal surface and in the bulk solution, respectively; ε repre-

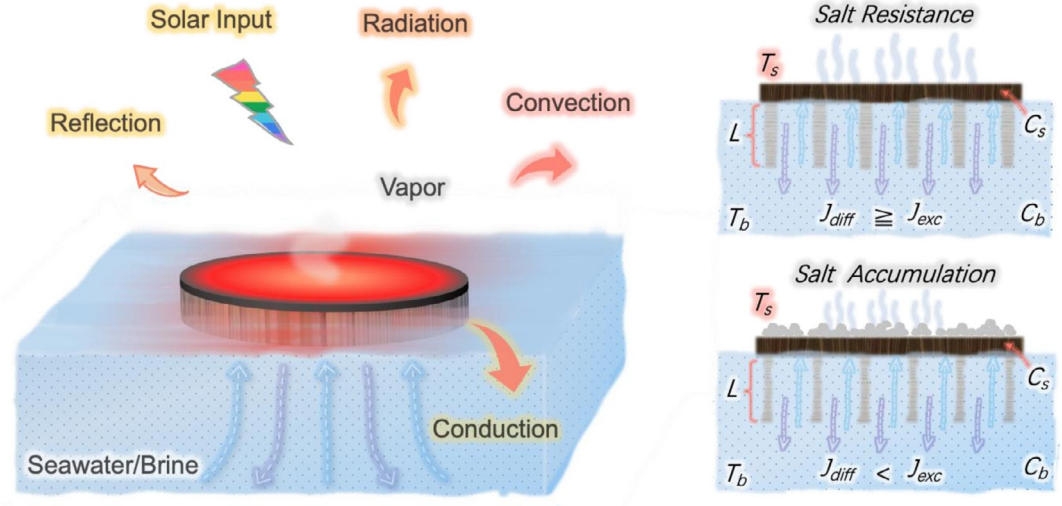

Fig. 3. Schematic diagram of salt resistance of the self-floating solar evaporator. During the interfacial evaporation process, the photothermal layer harvests light and converts it into heat energy. Seawater or brine with a temperature of T_b is transported to the evaporator surface along the aligned channels with a length of L and is heated at a temperature of T_s to generate vapor. At the same time, the evaporator may face energy losses caused by light reflection and heat loss (including radiation, convection, and conduction), as well as salt accumulation due to the lack of rapid ion diffusion. When the diffusion flux of the ion (J_{diff}) is larger than the rate of the salt excretion (J_{excr}), the evaporator will exhibit salt resistance, and if J_{diff} is lower than J_{excr}, salt will accumulate on the surface.

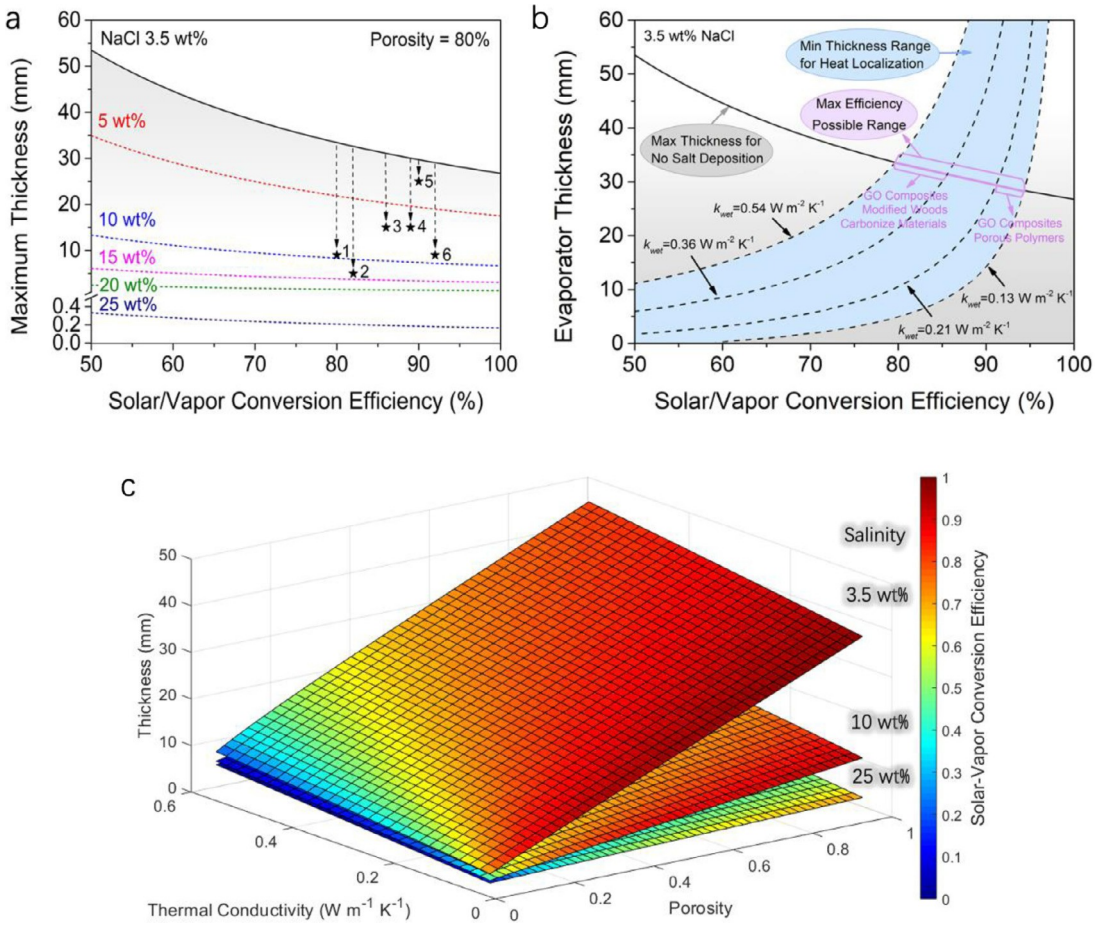

Fig. 4. a) Relationship between the solar/vapor conversion efficiency and the maximum thickness of the evaporator during vaporization of salt solutions with different concentrations (assuming porosity of 80%). The plots represent different self-floating evaporators which are used to treat 3.5 wt% NaCl solution under one sun irradiation. 1. Cellulose nanofiber/CNTs Janus evaporator (Hu et al., 2019); 2. Soot-deposited Janus cotton fabric (Gao et al., 2019); 3. Double layered MoS_2@sponge (Wang et al., 2020); 4. rGO/plant fiber sponge (Chen et al., 2018); 5. rGO/cotton fabric/PAN foam (Zhang et al., 2019b); 6. Fe_3Si aerogel/melamine foam (Zhang et al., 2018a). b) Trade-off analysis of the heat localization performance and the salt resistance of the evaporator. c) Relationship between the thickness, porosity, thermal conductivity of the evaporator and the efficiency. Three layers from top to bottom represent feed salinities of 3.5 wt%, 10 wt%, and 25wt% NaCl, respectively. (For interpretation of the references to colour in this figure legend, the reader is referred to the web version of this article.)

sents the porosity of the evaporator; τ denotes the tortuosity and L (m) corresponds with the length of the water channel.

Then, with a salt excretion rate on the evaporator J_{excr} (kg m^{-2} h^{-1}) under a specified light intensity q_{solar} (1000 W m^{-2}) and water evaporation rate J_{water} (kg m^{-2} h^{-1}), the solar-to-vapor energy conversion efficiency (η) is calculated as followed:

$$\eta = \frac{J_{water} h_{lv}}{E} \tag{2}$$

$$h_{lv} = h_{latent} \tag{3}$$

$$J_{exc} = \eta \frac{q_{solar}}{h_l} \times \frac{C_b}{\rho_{wate}} \tag{4}$$

In order to avoid salt accumulation, the diffusion flux of the ion (J_{diff}) should be larger than the rate of the salt excretion (J_{excr}), namely, $J_{diff} \geq J_{excr}$. Finally, we can obtain the following equation:

$$L \leq \frac{h_{lv} \rho_{water} \varepsilon D (C_s - C_b)}{\eta E \tau C_b} \tag{5}$$

Assuming a porosity (ε) of 80% and a tortuosity (τ) of 1, we then establish the relationship between maximum thickness (L) and energy conversion efficiency (η) in the solution with different bulk salt concentrations ranging from seawater salinity (3.5 wt%) to nearly saturated brine (25 wt%). As shown in **Fig. 4a**, as the concentration of the salt solution increases, in order to avoid salt accumulation, the thickness of the evaporator (or the length of the water channel) needs to be reduced accordingly to enhance the back-diffusion rate of ions from the evaporator to the bulk solu- tion. For example, when evaporating a 3.5 wt% NaCl solution, the maximum thickness needs to be less than 55 mm to eliminate the ion concentration and salt accumulation. We added some relevant data from the literature to verify the reliability of the model. The results indicated that the thicknesses of those evaporators which were capable of treating 3.5 wt% NaCl solution were below the theoretical maximum thickness. When the concentration increases to 25 wt%, the maximum thickness decreases significantly below 0.4 mm. Although the evaporator has a wide range of thicknesses to achieve salt resistance, the thicker evaporator will elongate the pathway of ion diffusion, negatively affecting the water transport along the aligned pores and thereby decreasing salt resistance and energy conversion efficiency.

Assuming the average thickness of the evaporator is 10 mm, we can establish the relationship between the porosity required and

the energy conversion efficiency (**Fig. S1**). In order to achieve an energy conversion efficiency higher than 50%, the maximum salt concentration that the evaporator can handle is less than 13 wt%, depending on the porosity of the evaporator. Therefore, if the salt concentration is increased further, the thickness also needs to be decreased appropriately.

Furthermore, considering the influence of the thickness on the heat loss, we used Fourier's Law to establish a relationship between the heat flux from the evaporator surface to the bulk water by conduction and the thickness of the evaporator. From this, we propose a simplified energy balance during stable evaporation:

$$q_{solar} = q_{evap} + q_{cond} = h_{lv}J_{water} + \frac{k(T_s - T_b)}{L} \quad (6)$$

When light reflected, radiative heat loss, and convective heat loss are ignored, the total input energy (q_{solar} =1000 W m^{-2}) is equal to the heat taken away by water evaporation at the stable evaporation stage (q_{evap}) and the conduction heat loss to the bulk solution (q_{cond}). h_{latent} (2.406 × 10^6 J kg^{-1}) and J_{water} (kg m^{-2} h^{-1}) is the vaporization enthalpy of water and evaporation rate at 40 °C, respectively. The temperature of the bulk solution was assumed to be 25 °C. Based on provided data from the reported literature (**Table S1**), k is considered the average thermal conductivities of the wet evaporator (0.4 W m^{-1} K^{-1}). In terms of 2D self-floating evaporators, we believe that there is a correlation between the water evaporation rate (J_{water}) and surface temperature (T_s) of the evaporator. Therefore, we provided a list of experimental data of reported literature in **Table S2**, including thermal conductivity of the evaporator, its surface temperature, evaporation rate, and energy conversion efficiency under specific light intensity. Through plotting the evaporation rate as a function of the surface temperature (**Fig. S2**), we can obtain a relationship between J_{water} and T_s:

$$J_{water} = 0.1372 \times T_s - 3.8966 \quad (7)$$

Then, combining the Eq. (6) and (7), T_s can be expressed as following:

$$q_{solar} = \frac{h_{lv}(0.1403T_s - 4.0103)}{3600} + \frac{k(T_s - 25)}{L} \quad (8)$$

$$T_s = \frac{3604.2 + 10L}{91.7 + 0.4L} \quad (9)$$

After that, we further obtain the relationship between the thickness (L) and the conduction heat loss (q_{cond})of different evaporators with different values of k (W m^{-1} K^{-1}), which can be represented as following:

$$q_{cond} = \frac{k \times (T_s - T_b)}{L} = \frac{1311.7k}{0.4 + 91.7L} \quad (10)$$

$$\eta = \frac{1000 - q_{cond}}{1000} \quad 100\% \quad (11)$$

It can be seen that the conduction heat loss is mainly affected by two factors, (1) the thermal conductivity and (2) the thickness of the wet evaporator. Combining with the relationship between energy conversion efficiency (η) and conduction heat loss (q_{cond}) in Eq. (11), materials with higher thermal conductivities (k) need to be thicker (L) to achieve higher heat localization and energy conversion efficiency, as shown by the dashed lines in **Fig. 4b**. However, this also increases the diffusion path of salt ions, which lowers the salinity of feedwater that can be treated without precipitation. For example, carbonized materials and wood-based evaporators with wet thermal conductivities (**Table S1**) close to the bulk water (0.6 W m^{-1} K^{-1}) may cause more energy loss if they are thinner. Meanwhile for GO composites and porous polymer-based evaporators with low thermal conductivities below 0.2 W m^{-1} K^{-1} in the wet state can significantly reduce heat dissipation.

Moreover, although **Fig. 4a** indicates that the thinner evaporator is more conducive to excreting solid salt, it also results in more heat conduction loss to the bulk solution. This establishes a trade-off between the energy conversion efficiency and the evaporator thickness. As shown in **Fig. 4b**, when the 3.5 wt% salt solution is evaporated, the solid lines and dashed lines represent the maximum thickness required for zero salt accumulation and the minimum thickness required for sufficient heat localization, respectively. The intersection of the two lines is the maximum energy conversion efficiency possible that the evaporator can achieve at the optimal thickness. As this optimal thickness depends on a variety of parameters-including feedwater salinity, porosity, and thermal conductivity-we developed a program that varied each parameter independently to find their influence on optimal evaporator thickness. In **Fig. 4c**, we developed surfaces that illustrate how the optimal thickness varies with porosity and thickness for three different feedwater salinities (3.5, 10, and 25 wt% NaCl). These surfaces are also color-coded by their solar-vapor conversion efficiencies, with warmer colors to indicate higher efficiencies. By looking at the top surface (feedwater salinity of 3.5 wt% NaCl), we can see the optimal thickness is strongly correlated with porosity, where higher porosities provide more channels for the back diffusion of salt. Meanwhile, low thermal conductivities enable better heat localization (with reduced conductive heat losses), thus improving the solar-vapor conversion efficiency. As feedwater salinity increases, the driving force for back diffusion is diminished, requiring lower optimal thicknesses to prevent scaling and causing lower solar-vapor conversion efficiencies from being achieved.

2.1.2. *Ion rejection and exchange*

In contrast to non-ionic (or neutral) hydrogels, such as PVA and poly- (N-isopropylacrylamide) (PNIPAM), ionic polyelectrolyte hydrogels with negatively-charged functional groups, such as poly (sodium acrylate) (PSA) and polystyrene sulfonate (PSS), can provide stronger interaction with water (Guo et al., 2020b), and have a higher osmotic pressure due to the accumulation of mobile counter ions, resulting in strong water absorption (Li et al., 2011). For instance, 20 wt% PSA hydrogel had a high osmotic pressure of 100 atm, which is more than twice the osmotic pressure of the PNIPAM hydrogel (Li et al., 2011; Ou et al., 2013). Additionally, Ma et al. found that the polyelectrolyte can effectively decrease the diffusion rate of ions ($Na^+ > Cl^- > K^+ > Mg^{2+}$) in a double-layer membrane-based evaporator with PSS-modified channels, and there was no salt deposition during the evaporation of a 3.5 wt% NaCl solution (Ma et al., 2019). Other studies indicated that the salt content in product water can be reduced by 23%~35% after swelling ionic polyelectrolyte hydrogels were dehydrated through mechanical force or light irradiation (Höpfner et al., 2010; Ali et al., 2015).

Considering the above advantages, Zeng et al. embedded a crosslinked PSA hydrogel in a microporous carbon foam and used it as an evaporator with ionic pumping effect for solar desalination (**Fig. 5**) (Zeng et al., 2019b). Under one-sun illumination, the hydrogel foam exhibited a stable water evaporation rate of roughly 1.3 LMH, and more than 80% Na^+ ions were blocked at the interface of 3.6 wt% NaCl solution and the foam. After continuous operation for 72-hours, the evaporation surface had no salt accumulation, especially in comparison with the pure foam in which water supply was only driven by capillary force. As we have previously summarized, the thickness of the evaporator is critical to improving the energy conversion efficiency. The thickness of the hydrogel foam affects both heat conduction loss and water absorption flux, which means that increasing the thickness can reduce heat losses but simultaneously increases water diffusion or flow resistance in the hydrogel. In this case, when the optimal thickness is found to be 5 mm, the energy conversion efficiency can reach 79%. As for ionic polyelectrolyte hydrogels, a high concentration of salt

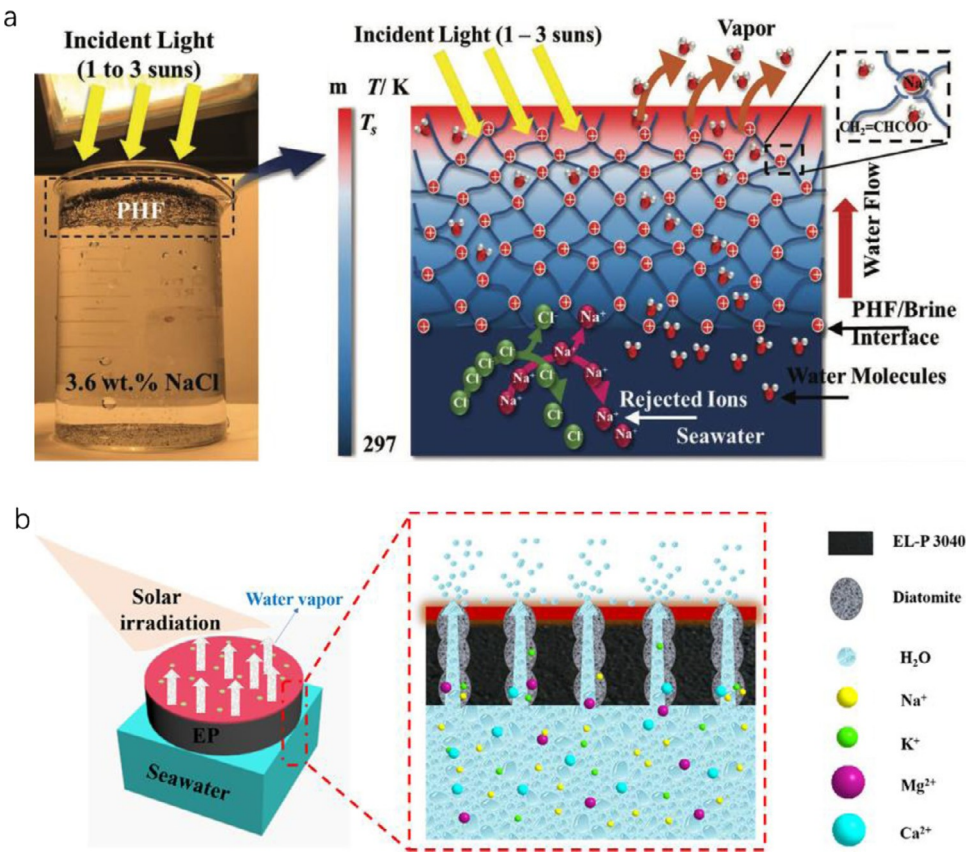

Fig. 5. (a) Self-floating P (SA) hydrogel foam and its experimental setup (Left); Water flow driven by the osmotic pressure gradient (ionic pumping), and salt-rejection effect due to charge repulsion and Donna potential (Right) (Zeng et al., 2019b). Copyright 2019, Wiley-VCH. (b) Schematic diagram of the solar desalination process and overcoming salt crystallization based on diatomite-regulated water supply (Liu et al., 2020). Copyright 2020, American Chemistry Society.

ions will reduce their osmotic pumping capabilities, but not affect the sufficient water supply driven by capillary flow. This work did not explore evaporator stability or desalination performance of the polyelectrolyte hydrogel-based evaporator when processing high-concentration saline.

Due to its excellent hydrophilicity, strong adsorption, and ion exchange capacity, natural inorganic diatomite is usually used to remove organic dyes and heavy metal ions (Khraisheh et al., 2004; Al-Degs et al., 2001; Erdem et al., 2005). Therefore, a self-floating evaporator which is made of diatomite modified with a conductive ink layer and porous melamine foam has been fabricated (Liu et al., 2020). The strong cation exchange capacity allows the evaporator with a thickness of 10 mm to handle 25 wt% NaCl solution for 10 h without any salt crystallization on the surface by inhibiting the transportation of salt ions. This has been attributed to sufficient water supplement avoiding ion accumulation and maintaining stable salinity levels inside the evaporator. Another consideration for materials with ion exchange capacity is that they require periodic replacement of the internally concentrated high-concentration salt ions (including monovalent and divalent ions). As a result, the recovery and reusability of these materials warrants further investigation to determine the limits of ion exchange capacity in long-term solar desalination applications.

2.2. *Transporter-assisted evaporator*

Transporter-assisted evaporators contain an additional two-dimensional water transporter (such as cotton yarns, air-laid paper, cellulose filter paper, glass fiber membrane, or various hydrophilic papers) to lift water to the evaporation surface through the capillary action (Han et al., 2020; Li et al., 2020; Zhang et al., 2020). As a result, these evaporators usually need to introduce a thermal insulation, such as polystyrene (PS) foam, as a support to hold photothermal materials. Due to low thermal conductivity (~0.03 W m^{-1} K^{-1}) of the PS foam, heat localization can be effectively enhanced. Our previous research further proved that the energy conversion efficiency of a GO photothermal leaf in the transporter-assisted evaporation configuration can be increased by 24% compared with that in the self-floating configuration. However, the indirect contact with the bulk solution is not conducive to rapid back diffusion of the concentrated salt ions. As the gradual accumulation of salt on the evaporation surface can lead to structural instability of the evaporator, measures should be taken to eliminate salt deposition or control salt crystallization.

2.2.1. *Physical cleaning*

Natural mangroves living in high-salinity environments can excrete excess salt from the stomata of the leaves through transpiration, and then use the rain to wash away the crystalline salt. Therefore, simulating this natural physical cleaning is an effective strategy to remove the crystalline layer from the evaporation surface. Our previous study indicated that a thick crystalline salt layer formed on a GO photothermal leaf during the evaporation of 15 wt% brine in a tree-like configuration for several days (**Fig. 6a**) (Finnerty et al., 2017a). After scraping off the salt and soaking in water for a period of time, the GO leaf could be cleaned and recovered. This simple method is suitable for renewing the performance of mechanically robust evaporation materials.

Recently, a direct-wash method has been proposed to accelerate the exfoliation and dissolution of the crystalline salt (**Fig. 6b**) (Jin et al., 2018; Zhu et al., 2019; Zhang et al., 2018). This treatment requires the material itself to possess excellent mechanical stability

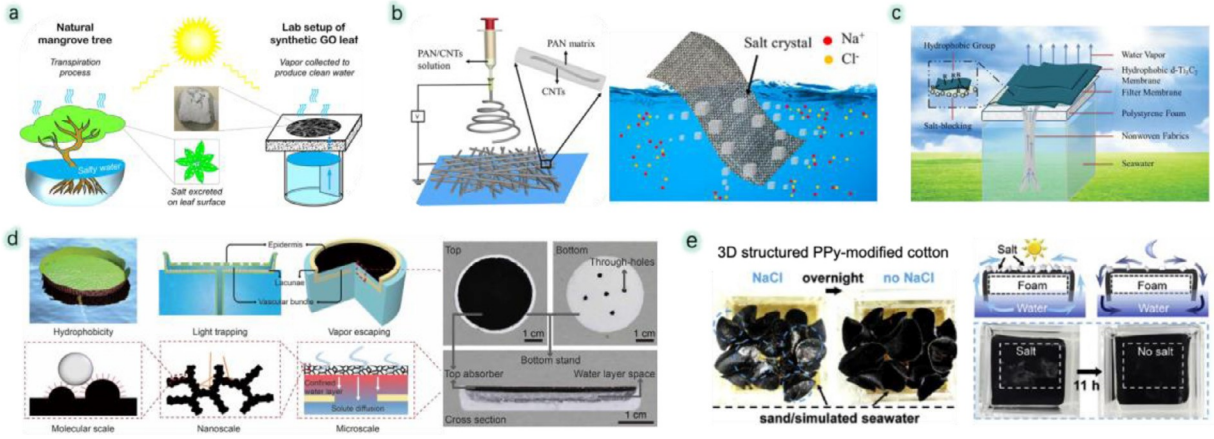

Fig. 6. The salt-resistant strategies of the transporter-assisted evaporator. Direct-wash method: a) Tree-like evaporation configuration with simulated natural transpiration (Mi et al., 2019; Finnerty et al., 2017a). Copyright 2017, American Chemistry Society. b) Flexible and washable CNT-embedded polyacrylonitrile (PAN) nonwoven fabric (Zhu et al., 2019). Copyright 2019, American Chemistry Society. Hydrophobic surface modification: c) Hydrophobic surface enabled salt-blocking 2D Ti_3C_2 MXene membrane (Zhao et al., 2018b). Copyright 2018, The Royal Society of Chemistry. d) Design concept and photographs of the water lily-inspired hierarchical structure (Xu et al., 2019a). Copyright 2019, AAAS. Periodic operation: e) Schematic illustration of 2D and 3D polypyrrole (PPy)/fibrous cotton evaporator structure and photos of the self-cleaning salt after one night (Xiao et al., 2019b). Copyright 2019, Elsevier. (For interpretation of the references to colour in this figure legend, the reader is referred to the web version of this article.)

and flexibility, otherwise the structural damage will lead to degradation of the photothermal material. A fiber cloth prepared by electrospinning provides a substrate to meet these requirements. By directly doping nano-sized photothermal materials (such as carbon nanotubes (CNTs) and carbon black) into hydrophilic polymer fibers with a diameter of several hundred nanometers, the wet cloth exhibited a light absorption capacity of more than 90% in the UV–vis-NIR region (350–2500 nm). Since the photothermal material is wrapped inside the nanofibers, repeated washing does not affect the light absorption and the evaporation performance. As far as practical applications are concerned, the electrospun fiber cloth has several advantages including simple preparation method, low cost, portability, ease of cleaning, good durability, and industrial mass production. However, for long-term evaporation of highly concentrated brine, the evaporation rate of the fiber cloth rapidly drops within a few hours unless manual cleaning is performed at regular intervals.

2.2.2. *Hydrophobic surface modification*

Notably, many natural plants and biological surfaces (such as lotus leaf and butterfly wings) possess superhydrophobic and self-cleaning properties due to the combination of low surface free energy and hierarchical surface structures (Barthlott and Neinhuis, 1997; Feng et al., 2002; Liu et al., 2014; Zheng et al., 2007). Inspired by this self-cleaning effect, various biomimetic materials have been developed and applied in environmental fields, such as oil/water separation (Wei et al., 2018; Sasmal et al., 2014; Dizge et al., 2019), oil absorption (Yang et al., 2018a; Yang et al., 2014; Zang et al., 2016; Li et al., 2016), membrane distillation (Liu et al., 2016a; Sun et al., 2019; Su et al., 2019), and water harvesting (Wang et al., 2017; Wen et al., 2018; Li et al., 2019a). For solar vapor generation, the superhydrophobic modification of the transporter-assisted evaporator have been performed to prevent the salt ions from passing through the photothermal layer (**Fig. 6c**). In order to obtain a hydrophobic surface, three methods are currently used: 1) applying hydrophobic inorganic photothermal nanomaterials (such as Al_2O_3 nanoparticles and CTSe nanospheres) (Yang et al., 2018b; Xu et al., 2019a); 2) combining hydrophobic polymers (such as poly (dimethylsiloxane) and polymethyl methacrylate) with photothermal materials (Xu et al., 2018; Liu et al., 2015); 3) post-treatment using low surface energy materials (such as hydrophobic silica nanoparticles, fluorosilane and beeswax) (Hu et al., 2019; Weng et al., 2018; Zhao et al., 2018b; Zhang et al., 2019d).

However, as transporter-assisted evaporator lack a fast ion back diffusion, the evaporation surface that is subjected to hydrophobic treatment cannot sustain its performance when evaporating highly concentrated brine over a long period of time. Therefore, Xu et al. designed a water lily-inspired hierarchical structure that can continuously treat 10 wt% brine under natural sunlight with a stable evaporation rate of about 1.27 kg m^{-2} h^{-1} for over 18 days (Xu et al., 2019a). They replaced the traditional 2D capillary channel with a drilled PS bottom support which allows water to go through and form a thin water layer under the superhydrophobic photothermal layer (**Fig. 6d**). During solar desalination, the concentrated ions are left behind the top layer and rapidly diffuse back to the bulk solution through the pores of the bottom support.

To sum up, combining the concept and mechanism of natural self-cleaning, the design of superhydrophobic surfaces is expected to be an active and energy-saving strategy to block the concentrated ions and leave them on the side of the membrane facing the salt solution, thereby achieving excellent salt resistance (Liu et al., 2015).

2.2.3. *Periodic operation*

In some regions where daily water demand is not very high, periodic operation can be employed to relieve salt fouling and recover the evaporator. This means that after sunset (or after turning off the light source), the accumulated salt crystals can dissolve and diffuse back into the bulk solution driven by the concentration gradient between the bulk solution and the photothermal layer (**Fig. 6e**) (Xu et al., 2018; Xu et al., 2019b; Ni et al., 2018; Li et al., 2019b; Zhang et al., 2019e; Xiao et al., 2019b). This is a slow, but passive cleaning strategy for the accumulated salt. Moreover, compared to the direct-washing method, the periodic operation strategy does not need robust photothermal materials, reducing labor and operating costs to a certain extent.

2.2.4. *Directed salt deposition*

Although the above methods can effectively reduce salt fouling, there are still limitations when processing highly concentrated brine. In this case, an alternative strategy is to control the location of crystallization on the evaporator, rather than eliminating

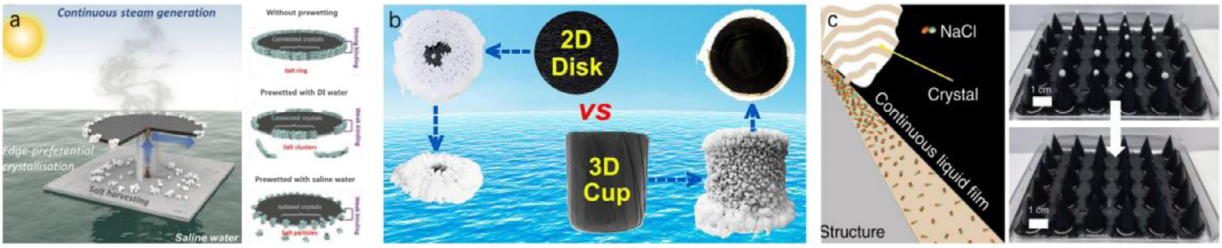

Fig. 7. Evaporator designs for controlled salt deposition. a) Schematic illustration of continuous solar vapor generation and edge-preferential crystallization of 2D evaporation disk (Xia et al., 2019). Copyright 2019, The Royal Society of Chemistry. b) NaCl crystallization comparison of 2D disk and 3D cup shaped solar evaporator (Shi et al., 2018). Copyright 2018, American Chemistry Society. c) Schemes of localized salt crystallization of biomimetic 3D solar evaporator based on a continuous DLP 3D printing system (left), and photos of removing salt crystals from the apex position of the arrayed evaporator after solar-driven water evaporation (right) (Wu et al., 2020). Copyright 2020, Springer Nature.

salt crystals, which minimizes the negative effects of salt deposition on the evaporation surface.

Xia et al. investigated the relationship between the water transport capacity and the evaporation rate to effectively control the position of salt crystallization on the photothermal membrane (Xia et al., 2019). They found that the salt concentration of the residual solution gradually increased as it approached the edge of the evaporator (**Fig. 7a**). When the replenished water cannot dilute the concentrated solution in time, a crystalline salt ring forms on the hydrophilic evaporation disk. As long as the radius of the evaporation disk is smaller than the radius of the salt ring, the salt crystals tend to form at the edge of the disk and naturally fall off due to gravity. However, the salt ring disappeared while evaporating mixed salt solutions containing divalent ions (such as magnesium chloride and calcium chloride) due to their lower solubilities. Therefore, this method is not suitable for evaporating actual seawater unless pre-treatment is performed.

In order to mitigate the effects of salt scaling for transporter-assisted evaporators, Shi et al. designed a three-dimensional (3D) paper cup shaped evaporator that allowed the salt to precipitate and crystallize on the outer surface, while the inner wall can undergo photothermal conversion and evaporation (**Fig. 7b**) (Shi et al., 2018). They demonstrated that with a given configuration, their evaporator could withstand inlet salt concentrations up to 20 wt% NaCl, taking advantage of humidity and temperature differences between the inner wall and the outer wall of the cup to control the crystallization position. Although a small amount of salt crystals appears at the bottom of the cup when evaporating the high-concentration brine (>20%), the evaporation rate can be maintained at 1.3 kg m^{-2} h^{-1} for 120 min.

Especially for transporter-assisted evaporators treating highly concentrated brines, it is difficult to achieve a high evaporation rate due to lower vapor pressure of brines and increased liquid viscosities associated with concentrating brine. Recently, Wu et al. designed a bio-mimetic, 3D-printed evaporator that has a high evaporation rate of 2.24 kg m^{-2} h^{-1} with energy efficiency of 97.1% when self-floating in 25 wt% NaCl solution (**Fig. 7c**) (Wu et al., 2020). Importantly, each cone of the evaporator forms a temperature gradient along the slope under vertical illumination. The absorbed water forms a continuous liquid film with uneven thickness on the surface via the Marangoni effect, resulting in localized salt crystallization on the apex of each cone. Due to very small coverage of the solid salt, the evaporator is able to maintain stable evaporation performance, while the deposited salt on the 3D evaporator can be easily removed.

In summary, the strategy of controlling salt crystallization can help with obtaining valuable fresh water while capturing a large quantity of the by-product, crystalline salt. Therefore, this strategy is particularly suitable for outdoor evaporation ponds with high salinity, which not only achieves zero liquid discharge, but also increases extra economic benefits.

2.2.5. *Crossflow*

Cotton products are made up of thousands of hydrophilic yarns with many tiny spaces between them, which endow them with excellent capillary action and wicking effect. For example, a cotton rod or strand can be immersed into the bulk water and directly used as transport channels to pump water (Xu et al., 2018; Wu et al., 2019). As for thin cotton fabric or cloth, its surface can be modified with a variety of photothermal materials, including PPy (Xiao et al., 2019b), MoS_2 (Guo et al., 2018), and CNTs (Qi et al., 2020). The black composite material can quickly absorb water and generate vapor under simulated light or outdoor conditions. For example, Ni et al. designed a multiple floating solar still with excellent salt-rejection ability (**Fig. 8a**) (Ni et al., 2018). A black cellulose fabric was used to harvest light and wick water, while several PS foams were arranged at intervals as a bottom support to achieve thermal insulation and salt excretion. To demonstrate the salt-rejection ability of the solar still, additional solid salt was placed on the surface to saturate the fabric during the evaporation of 3.5 wt% NaCl simulated seawater. The salt completely dissolved and ion concentration in the fabric decreased and approached the bulk solution after 20 h of one-sun illumination. However, a large fabric wick area (~20%) might dissipate heat to the bulk solution along with the diffusion process, resulting in a lower solar-to-vapor energy conversion efficiency of about 56%.

In order to reduce heat conduction loss of traditional floating evaporation systems, Liu et al. proposed an indirect-contact evaporation system by hanging a polyaniline (PANi)-cotton fabric in air and immersing its two edges in water (**Fig. 8b**) (Liu et al., 2019). Air is an excellent thermal insulator with a low thermal conductivity (~0.023 W m^{-1} K^{-1}), resulting in a high energy conversion efficiency (~90%). Additionally, double evaporation surfaces can facilitate the vapor diffusion, and even when evaporating 21 wt% NaCl solution, the hanging evaporation system still had a high evaporation rate of 1.9 kg m^{-2} h^{-1}. Importantly, the two edges continuously replenished water by wicking effect, so no salt accumulation was observed on the surface of the arc-shape fabric, while extra concentrated brine as liquid by-product can be collected in a container. In contrast, the flat fabric was not conducive for avoiding salt scaling, thereby causing a decrease in the evaporation rate.

Moreover, the results indicated that the drop speed of brine had an impact on the salt accumulation and energy efficiency. The fast drop speed (0.4~56 g L^{-1}) could eliminate salt accumulation but increases heat loss (0%~24.5% of the total incident solar energy) and reduces vapor recovery efficiency (95%~9.09%). The indirect-contact evaporation design combing with crossflow strategy not only solves the problem of salt crystallization caused by the 2D planar evaporator, but also broadens the application scenarios of evaporators, making it possible to carry out large-scale offshore solar-driven desalination.

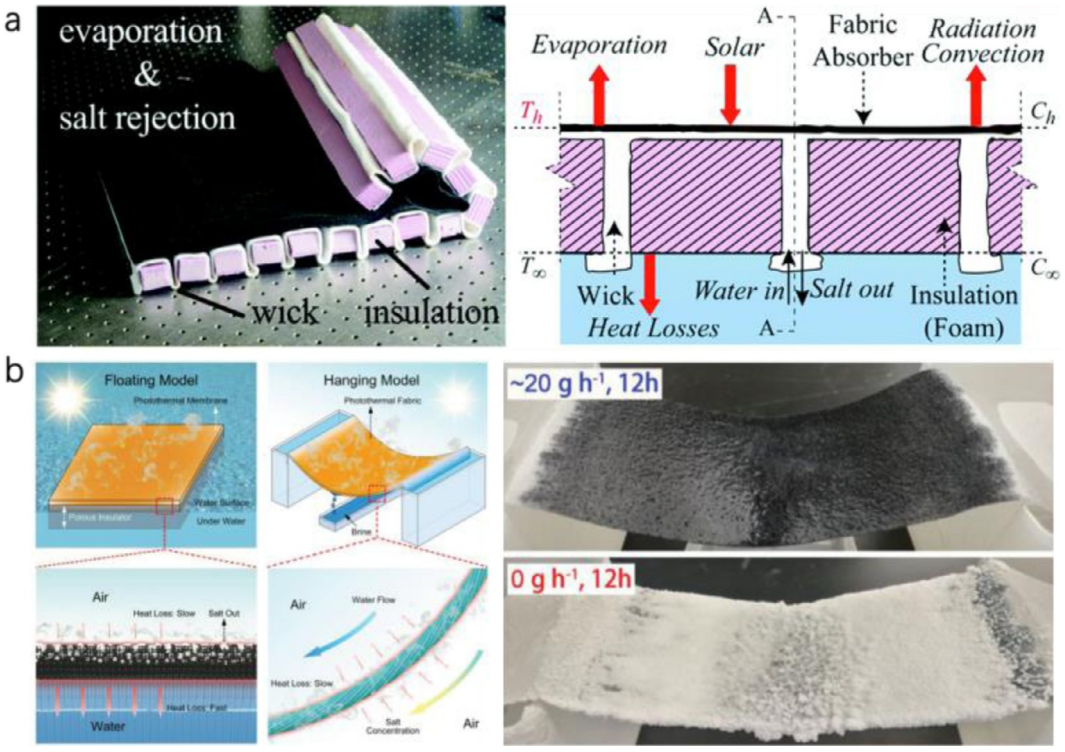

Fig. 8. a) A salt-rejecting floating evaporation structure comprised of a composite fabric wick and polystyrene foam insulation (Ni et al., 2018). Copyright 2018, The Royal Society of Chemistry. b) Schematic illustration of seawater evaporation in the floating photothermal membrane and hanging photothermal fabric and photographs of salt resistance (Liu et al., 2019). Copyright 2019, Wiley-VCH.

3. Conclusion and outlook

3.1. Conclusion

In order to clearly show the ability of using various strategies to solve salt scale formation, we summarized the current interfacial evaporation performance based on the reported research, including materials, feedwater salinity, evaporation rate, energy conversion efficiency, duration and reusability. We draw the following conclusions according to Table 1: (1) Drilled wood and hydrogel-based self-floating evaporators can stably process NaCl solutions exceeding 20 wt% and run continuously for about 100 h without depositing salt. By constructing artificially aligned channels inside the polymeric or inorganic foam, the self-floating evaporator can achieve long-term salt resistance (240 h for 3.5 wt% NaCl) with a high energy-conversion efficiency of over 80%. Obviously, the self-floating evaporator with appropriate materials and well-designed structure not only has excellent stable desalination performance, but also is suitable for cost-effective and decentralization treatment of seawater and industrial brine. (2) Using the ion repulsion effect of the ionic hydrogel to remove ions is a novel strategy to resist salt deposition and obtain stable water evaporation. However, the low osmotic pressure of ionic hydrogels limits the ability of the evaporator to handle high-concentration salt solutions. (3) The evaporator with ion exchange capacity can continuously process 25 wt% NaCl solution for 10 h. However, failure to achieve regeneration and reusability will shorten life span of the evaporator and increase material and operation costs. Therefore, this strategy still needs to be further studied. (4) An evaporator with a hydrophobic surface can continuously evaporate 10 wt% NaCl solution for up to 100 h. At the same time, poor wettability may result in slow evaporation rate and low energy-conversion efficiency. In addition, the hydrophobic surface constructed by fluorine-containing chemical reagents may not only increases the material cost, but also cause potential environmental pollution during the preparation or operation process. (5) When periodic operation and physical cleaning are used, the operation duration of the evaporator depends on the feedwater salinity and the change in evaporation area caused by salt accumulation. Therefore, the two strategies may not be suitable for areas and applications with intensive water demand. (6) The direct deposition strategy enables the evaporator to handle highly concentrated brine, and the salt accumulation position does not significantly affect its light absorption area, thereby extending the operating time up to 600 h. This strategy can be used for the treatment of concentrated brine discharged by RO and evaporation ponds of chemical plants, so that salt by-products can be obtained while improving the recovery rate of water, thereby achieving the goal of zero liquid discharge. (7) The evaporators with fast cross-flow effect can handle 21 wt% NaCl solution by accelerating ion diffusion. And the unique evaporation configuration is suitable for offshore desalination and water treatment.

Additionally, a schematic diagram is provided to illustrate the advantages and difficulties of different strategies in the self-floating and transporter-assisted evaporation configurations, as well as the feedwater salinity that can be handled (**Fig. 9**). Based on the data and summary, we reach the following conclusions:

(1) Both evaporation configurations can handle feedwater with a wide range of salinity and exhibit excellent evaporation performance.
(2) When rationally designed—taking into account the structural and physical properties (e.g., material, thickness, porosity, and thermal conductivity)—each self-floating evaporator has an upper operation limit of NaCl concentration without salt deposition, correlating with a possible maximum solar/vapor conversion efficiency.
(3) Regarding ion exclusion and exchange strategies for self-floating evaporators, although the operation limit of salinity is as high

Table 1
A summary of optimal evaporation performance using different strategies in the self-floating and transporter-assisted evaporator.

Configuration	Strategy	Typical Materials (Thickness)	Current Optimal Performance					References
			Max. Salinity (wt% NaCl)	Rate (kg m^{-2} h^{-1})	Efficiency (η%)	Duration (h)	Recovery Reusability	
Self-floating evaporator	Back diffusion	Hybrid hydrogels (5 mm)	25	1.6	>90	96	√	(Zhou et al., 2018)
		Drilled Wood (20 mm)	20	1.04	75	100	√	(Kuang et al., 2019)
		Hydrophilic foams with artificial channels (25 mm)	3.5	1.47	90	240	√	(Zhang et al., 2019b)
	Back diffusion & Hydrophobic modification	Foams with artificial channels (9 mm)	12	1.2	80	100	√	(Hu et al., 2019)
	Ion rejection	Ionic hydrogels (5 mm)	3.6	1.2	79	72	–	(Zeng et al., 2019b)
	Ion exchange	Natural diatomite (10 mm)	25	–	–	10	–	(Liu et al., 2020)
Transporter-assisted evaporator	Hydrophobic modification	Lily-inspired structure	10	1.28	78.5	8	√	(Xu et al., 2019a)
	Periodic operation	Filter paper	3.5	1.42	<90	8	√	(Xu et al., 2019b)
	Physical cleaning	Porous filter	15	0.5	–	120	√	(Finnerty et al., 2017b)
	Directed salt deposition	2D filter disk	3.5	1.42	81.2	600	√	(Xia et al., 2019)
		3D-print evaporator	25	2.24	97.1	9	√	(Wu et al., 2020)
	Crossflow	Hanging arc-shape fabric	21	1.9	89.9	12	√	(Liu et al., 2019)

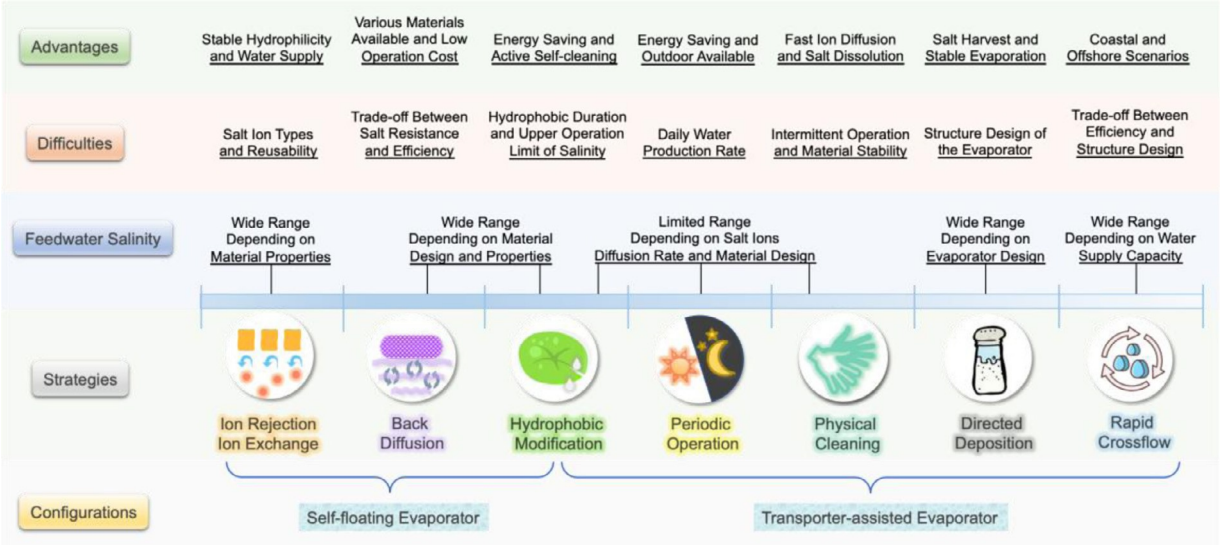

Fig. 9. Schematic illustration of advantages and difficulties of various strategies of solving scaling in the self-floating evaporator and transporter-assisted evaporator and the salinity of the feedwater that can be handled.

as 25 wt%, their recoverability, reusability, and desalination performance have not been fully investigated when processing salt solution containing divalent ions or realistic seawater matrices.

(4) Regardless of the evaporation configuration, hydrophobic modification is a feasible strategy to prevent salt ions from passing through the evaporation layer. However, in long-term evaporation processes or outdoor operation, it is necessary to investigate the hydrophobic durability and the maximum operation salinity of the evaporator.

(5) Periodic operation and physical washing are quite simple and convenient methods to remove salt crystals on the evaporation surface, although this approach is less effective for transporter-assisted evaporators, resulting in lower daily water production rate and increased operation costs.

(6) If the structure of the transporter-assisted evaporator is properly designed, the crystalline salt will be directly deposited at the desired location, and it can be collected as a by-product without affecting the evaporation performance.

(7) The rapid crossflow established inside the evaporator can also effectively alleviate salt accumulation during the evaporation of high-concentration brine. The trade-off between energy conversion efficiency and evaporator design, however, needs to be considered to minimize heat loss.

3.2. Outlook

Compared with other traditional desalination and water purification methods (such RO, ultrafiltration), interfacial solar-driven

vapor generation is a sustainable, energy-saving technology, operating without the emission of greenhouse gases. So far, it has presented broad application prospects in the treatment of industrial wastewater containing biological, chemical contaminants, and the desalination of seawater or brine (Zhao et al., 2020; Tao et al., 2018). For example, in terms of the removal of the bacteria in the wastewater, nanomaterials like ZnO nanoparticles and MXene nanosheets are added to the evaporator to enhance the antibiofouling performance (Zha et al., 2019; Wang et al., 2019c). Chemical pollutants (e.g., rhodamine B, nitrobenzene, and carbamazepine) can be degraded by the addition of functional nanomaterials (e.g., TiO_2 nanoparticles and MoS_2 nanosheets) in the photothermal layer through photocatalytic reactions (Chen et al., 2019; Liu et al., 2016b; Lou et al., 2016). However, salt accumulation on the evaporator is still a significant challenge during long-term evaporation or for the treatment of highly concentrated brines. Therefore, different evaporation systems and a variety of structural designs have been used and studied to realize zero-salt deposition or controlled salt crystallization, thereby improving the evaporation performance and extending service life. Although we have proposed a preliminary framework for analyzing the effect of thermal conductivity, porosity, and thickness for self-floating evaporation systems, further research is needed to develop a deeper understanding on the behavior of dissolved salt within the evaporator. This is especially true near the evaporative interface within solar evaporators, where high salt concentrations are suspected to impact evaporation rates, even without precipitation. Furthermore, research is needed to explore the scaling effects of different scaling species and complex mixtures of dissolved salts. Currently, a majority of this work has focused on the scaling effects of sodium chloride, which has a relatively high solubility and unique behavior compared to other species. Finally, an advantage of interfacial solar vapor generation is its passive operation. Therefore, passive salt management strategies would be ideal for extending the operating life of these evaporators. Although transporter-assisted and 3D evaporators have inherent thermal insulation and can effectively reduce heat conduction loss, they lack rapid ion back diffusion along the 2D water channels, limiting this long-term operation. Therefore, salt management needs to be an integral consideration when designing these systems. It is evident that as interfacial solar vapor generation begins to mature into various desalination and water treatment technologies, developing effective salt management strategies will continue to be critical area of research for optimizing the performance of photothermal evaporators.

Declaration of Competing Interest

We declare that we do not have any commercial or associative interest that represents a conflict of interest in connection with the manuscript.

Acknowledgements

This research is supported by U. S. National Science Foundation (NSF) under award nos. CBET-1565452 and CBET-1706059. L. Z. is grateful for the support from the China Scholarship Council (CSC) Graduate fellowship. However, the opinions expressed herein are those of the authors and do not necessarily reflect those of the sponsors.

References

Ali, W., Gebert, B., Hennecke, T., Graf, K., Ulbricht, M., Gutmann, J.S., 2015. Design of thermally responsive polymeric hydrogels for brackish water desalination: effect of architecture on swelling, deswelling, and salt rejection. ACS Appl. Mater. Interfaces 7 (29), 15696–15706.

Al-Degs, Y., Khraisheh, M., Tutunji, M., 2001. Sorption of lead ions on diatomite and manganese oxides modified diatomite. Water Res. 35 (15), 3724–3728.

Barthlott, W., Neinhuis, C., 1997. Purity of the sacred lotus, or escape from contamination in biological surfaces. Planta 202 (1), 1–8.

Cai, Y., Shen, W., Loo, S.L., Krantz, W.B., Wang, R., Fane, A.G., Hu, X., 2013. Towards temperature driven forward osmosis desalination using Semi-IPN hydrogels as reversible draw agents. Water Res. 47 (11), 3773–3781.

Chen, R., Wang, X., Gan, Q.M., Zhang, T.Q., Zhu, K.H., Ye, M.M., 2019. A bifunctional MoS2-based solar evaporator for both efficient water evaporation and clean freshwater collection. J. Mater. Chem. A 7 (18), 11177–11185.

Chen, T.J., Wang, S., Wu, Z.Z., Wang, X.D., Peng, J., Wu, B.H., Cui, J.Q., Fang,, X.L., Xiec, Y.Q., 2018. A Cake Making Strategy to Prepare Reduced Graphene Oxide Wrapped Plant Fiber Sponges for High-efficiency Solar Steam Generation. J. Mater. Chem. A 6 (30), 14571–14576.

Chen, X.M., Wu, J., Ma, R.Y., Hua, M., Koratkar, N., Yao, S.H., Wang, Z.K., 2011. Nanograssed Micropyramidal Architectures for Continuous Dropwise Condensation. Adv. Funct. Mater. 21 (24), 4617–4623.

Dizge, N., Shaulsky, E., Karanikola, V., 2019. Electrospun cellulose nanofibers for superhydrophobic and oleophobic membranes. J. Memb. Sci. 590.

Durkaieswaran, P., Murugavel, K.K., 2015. Various special designs of single basin passive solar still - A review. Renewable Sustainable Energy Rev. 49, 1048–1060.

Erdem, E., Çölgeçen, G., Donat, R., 2005. The removal of textile dyes by diatomite earth. J. Colloid Interface Sci. 282 (2), 314–319.

Feng, L., Li, S., Li, Y., Li, H., Zhang, L., Zhai, J., Song, Y., Liu, B., Jiang, L., Zhu, D, 2002. Super-hydrophobic surfaces: from natural to artificial. Adv. Mater. 14 (24), 1857–1860.

Fang, Q., Li, T., Chen, Z., Lin, H., Wang, P., Liu, F., 2019. Full biomass-derived solar stills for robust and stable evaporation to collect clean water from various wa- ter-bearing media. ACS Appl. Mater. Interfaces 11 (11), 10672–10679.

Finnerty, C., Zhang, L., Sedlak, D.L., Nelson, K.L., Mi, B.X., 2017a. Synthetic Graphene Oxide Leaf for Solar Desalination with Zero Liquid Discharge. Environ. Sci. Technol. 51 (20), 11701–11709.

Finnerty, C., Zhang, L., Sedlak, D.L., Nelson, K.L., Mi, B., 2017b. Synthetic graphene oxide leaf for solar desalination with zero liquid discharge. Environ. Sci. Technol. 51 (20), 11701–11709.

Guo, Y., Zhao, F., Zhou, X., Chen, Z., Yu, G., 2019a. Tailoring Nanoscale Surface Topography of Hydrogel for Efficient Solar Vapor Generation. Nano Lett. 19 (4), 2530–2536.

Guo, Y., Zhou, X., Zhao, F., Bae, J., Rosenberger, B., Yu, G., 2019b. Synergistic Energy Nanoconfinement and Water Activation in Hydrogels for Efficient Solar Water Desalination. ACS Nano 13 (7), 7913–7919.

Guo, Y., Lu, H., Zhao, F., Zhou, X., Shi, W., Yu, G., 2020a. Biomass-Derived Hybrid Hydrogel Evaporators for Cost-Effective Solar Water Purification. Adv. Mater. 32 (11), 1907061.

Gao, S., Dong, X., Huang, J., Dong, J., Maggio, F.D., Wang, S., Guo, F., Zhu, T., Chen, Z., Lai, Y., 2019. Bioinspired Soot-Deposited Janus Fabrics for Sustainable Solar Steam Generation with Salt-Rejection.. Global Challenges 3 (8), 1800117.

Guo, Y., Bae, J., Fang, Z., Li, P., Zhao, F., Yu, G., 2020b. Hydrogels and Hydro- gel-Derived Materials for Energy and Water Sustainability. Chem. Rev. 120 (15), 7642–7707.

Guo, Z., Wang, G., Ming, X., Mei, T., Wang, J., Li, J., Qian, J., Wang, X., 2018. PEGylated self-growth MoS2 on a cotton cloth substrate for high-efficiency solar energy utilization. ACS Appl. Mater. Interfaces 10 (29), 24583–24589.

Han, X., Zang, L., Zhang, S., Dou, T., Li, L., Yang, J., Sun, L., Zhang, Y., Wang, C., 2020. Hydrophilic polymer-stabilized porous composite membrane for water evaporation and solar desalination. RSC Adv. 10 (5), 2507–2512.

Hartanto, Y., Zargar, M., Wang, H., Jin, B., Dai, S., 2016. Thermoresponsive acidic microgels as functional draw agents for forward osmosis desalination. Environ. Sci. Technol. 50 (8), 4221–4228.

He, S., Chen, C., Kuang, Y., Mi, R., Liu, Y., Pei, Y., Kong, W., Gan, W., Xie, H., Hitz, E., 2019. Nature-inspired salt resistant bimodal porous solar evaporator for efficient and stable water desalination. Energy Environ. Sci. 12 (5), 1558–1567.

Höpfner, J., Klein, C., Wilhelm, M., 2010. A novel approach for the desalination of seawater by means of reusable poly (acrylic acid) hydrogels and mechanical force. Macromol. Rapid Commun. 31 (15), 1337–1342.

Hou, Y.M., Yu, M., Chen, X.M., Wang, Z.K., Yao, S.H., 2015. Recurrent Filmwise and Dropwise Condensation on a Beetle Mimetic Surface. ACS Nano 9 (1), 71–81.

Hu, R., Zhang, J., Kuang, Y., Wang, K., Cai, X., Fang, Z., Huang, W., Chen, G., Wang, Z., 2019. A Janus evaporator with low tortuosity for long-term solar desalination. J. Mater. Chem. A 7 (25), 15333–15340.

Khraisheh, M.A., Al-degs, Y.S., Mcminn, W.A., 2004. Remediation of wastewater containing heavy metals using raw and modified diatomite. Chem. Eng. J. 99 (2), 177–184.

Kuang, Y., Chen, C., He, S., Hitz, E.M., Wang, Y., Gan, W., Mi, R., Hu, L., 2019. A High--Performance Self-Regenerating Solar Evaporator for Continuous Water Desalination. Adv. Mater. 31 (23), 1900498.

Jin, Y., Chang, J., Shi, Y., Shi, L., Hong, S., Wang, P., 2018. A highly flexible and washable nonwoven photothermal cloth for efficient and practical solar steam generation. J. Mater. Chem. A 6 (17), 7942–7949.

Liang, H., Liao, Q., Chen, N., Liang, Y., Lv, G., Zhang, P., Lu, B., Qu, L., 2019. Thermal efficiency of solar steam generation approaching 100% through capillary water transport. Angew. Chem..

Li, L., Zang, L., Zhang, S., Dou, T., Han, X., Zhao, D., Zhang, Y., Sun, L., Zhang, Y., 2020. GO/CNT-silica Janus nanofibrous membrane for solar-driven interfacial steam generation and desalination. J. Taiwan Inst. Chem. Eng. 111, 191–197.

Li, D., Zhang, X., Yao, J., Simon, G.P., Wang, H., 2011. Stimuli-responsive polymer hydrogels as a new class of draw agent for forward osmosis desalination. Chem. Commun. 47 (6), 1710–1712.

Li, J., Yan, L., Tang, X.H., Feng, H., Hu, D.C., Zha, F., 2016. Robust Superhydrophobic Fabric Bag Filled with Polyurethane Sponges Used for Vacuum-Assisted Continuous and Ultrafast Absorption and Collection of Oils from Water. Adv. Mater. Interfaces 3 (9).

Li, D.K., Wang, Z.T., Wu, D.H., Han, G.C., Guo, Z.G., 2019a. A hybrid bioinspired fiber trichome with special wettability for water collection, friction reduction and self-cleaning. Nanoscale 11 (24), 11774–11781.

Li, T., Fang, Q., Xi, X., Chen, Y., Liu, F., 2019b. Ultra-robust carbon fibers for multi–media purification via solar-evaporation. J. Mater. Chem. A 7 (2), 586–593.

Liu, H., Chen, C., Chen, G., Kuang, Y., Zhao, X., Song, J., Jia, C., Xu, X., Hitz, E., Xie, H., 2018. High-performance solar steam device with layered channels: artificial tree with a reversed design. Adv. Energy Mater. 8 (8), 1701616.

Liu, K.-.K., Jiang, Q., Tadepalli, S., Raliya, R., Biswas, P., Naik, R.R., Singamaneni, S., 2017. Wood–graphene oxide composite for highly efficient solar steam generation and desalination. ACS Appl. Mater. Interfaces 9 (8), 7675–7681.

Liu, C., Cai, C., Zhao, X., 2020. Overcoming Salt Crystallization During Solar Desalination Based on Diatomite Regulated Water Supply. Acs Sustainable Chemistry & Engineering.

Liu, Q.L., Liu, C.H., Zhao, L., Ma, W.C., Liu, H.L., Ma, J., 2016a. Integrated forward osmosis-membrane distillation process for human urine treatment. Water Res. 91, 45–54.

Liu, Y.M., Chen, J.W., Guo, D.W., Cao, M.Y., Jiang, L., 2015. Floatable, Self-Cleaning, and Carbon-Black-Based Superhydrophobic Gauze for the Solar Evaporation Enhancement at the Air-Water Interface. ACS Appl. Mater. Interfaces 7 (24), 13645–13652.

Liu, K., Cao, M., Fujishima, A., Jiang, L., 2014. Bio-inspired titanium dioxide materials with special wettability and their applications. Chem. Rev. 114 (19), 10044–10094.

Liu, Z., Wu, B., Zhu, B., Chen, Z., Zhu, M., Liu, X., 2019. Continuously Producing Watersteam and Concentrated Brine from Seawater by Hanging Photothermal Fabrics under Sunlight. Adv. Funct. Mater. 1905485.

Liu, Y., Lou, J.W., Ni, M.T., Song, C.Y., Wu, J.B., Dasgupta, N.P., Tao, P., Shang, W., Deng, T., 2016b. Bioinspired Bifunctional Membrane for Efficient Clean Water Generation. ACS Appl. Mater. Interfaces 8 (1), 772–779.

Lou, J., Liu, Y., Wang, Z., Zhao, D., Song, C., Wu, J., Dasgupta, N., Zhang, W., Zhang, D., Tao, P., 2016. Bioinspired multifunctional paper-based rGO composites for solar–driven clean water generation. ACS Appl. Mater. Interfaces 8 (23), 14628–14636.

Ma, X., Fang, W., Guo, Y., Li, Z., Chen, D., Ying, W., Xu, Z., Gao, C., Peng, X., 2019. Hierarchical Porous SWCNT Stringed Carbon Polyhedrons and PSS Threaded MOF Bilayer Membrane for Efficient Solar Vapor Generation. Small 15 (15), 1900354.

Mi, B., Finnerty, C., Conway, K., 2019. Prospects of artificial tree for solar desalination. Curr. Opin. Chem. Eng. 25, 18–25.

Ni, G., Zandavi, S.H., Javid, S.M., Boriskina, S.V., Cooper, T.A., Chen, G., 2018. A salt-rejecting floating solar still for low-cost desalination. Energy Environ. Sci. 11 (6), 1510–1519.

Ou, R., Wang, Y., Wang, H., Xu, T., 2013. Thermo-sensitive polyelectrolytes as draw solutions in forward osmosis process. Desalination 318, 48–55.

Puperi, D.S., Kishan, A., Punske, Z.E., Wu, Y., Cosgriff-Hernandez, E., West, J.L., Grande-Allen, K.J., 2016. Electrospun polyurethane and hydrogel composite scaffolds as biomechanical mimics for aortic valve tissue engineering. ACS Biomater. Sci. Eng. 2 (9), 1546–1558.

Qi, H., Cao, J., Xin, Y., Mao, X., Xie, D., Luo, J., Chu, B., 2017. Dual responsive zein hydrogel membrane with selective protein adsorption and sustained release property. Mater. Sci. Eng. C 70, 347–356.

Qi, Q., Wang, Y., Wang, W., Ding, X., Yu, D, 2020. High-efficiency solar evaporator prepared by one-step carbon nanotubes loading on cotton fabric toward water purification. Sci. Total Environ. 698, 134136.

Qian, X., Zhao, Y., Alsaid, Y., Wang, X., Hua, M., Galy, T., Gopalakrishna, H., Yang, Y., Cui, J., Liu, N., Marszewski, M., Pilon, L., Jiang, H., He, X., 2019. Artificial phototropism for omnidirectional tracking and harvesting of light. Nat. Nanotechnol. 14 (11), 1048–1055.

Razmjou, A., Barati, M.R., Simon, G.P., Suzuki, K., Wang, H., 2013a. Fast deswelling of nanocomposite polymer hydrogels via magnetic field-induced heating for emerging FO desalination. Environ. Sci. Technol. 47 (12), 6297–6305.

Razmjou, A., Liu, Q., Simon, G.P., Wang, H., 2013b. Bifunctional polymer hydrogel layers as forward osmosis draw agents for continuous production of fresh water using solar energy. Environ. Sci. Technol. 47 (22), 13160–13166.

Sasmal, A.K., Mondal, C., Sinha, A.K., Gauri, S.S., Pal, J., Aditya, T., Ganguly, M., Dey, S., Pal, T., 2014. Fabrication of superhydrophobic copper surface on various substrates for roll-off, self-cleaning, and water/oil separation. ACS Appl. Mater. Interfaces 6 (24), 22034–22043.

Shi, Y., Zhang, C.L., Li, R.Y., Zhuo, S.F., Jin, Y., Shi, L., Hong, S., Chang, J., Ong, C.S., Wang, P., 2018. Solar Evaporator with Controlled Salt Precipitation for Zero Liquid Discharge Desalination. Environ. Sci. Technol. 52 (20), 11822–11830.

Sun, Z., Li, W., Song, W., Zhang, L., Wang, Z., 2020. A high-efficiency solar desalination evaporator composite of corn stalk, Mcnts and TiO 2: ultra-fast capillary water moisture transportation and porous bio-tissue multi-layer filtration. J. Mater. Chem. A 8 (1), 349–357.

Sun, M., Boo, C., Shi, W.B., Rolf, J., Shaulsky, E., Cheng, W., Plata, D.L., Qu, J.H., Elimelech, M., 2019. Engineering Carbon Nanotube Forest Superstructure for Robust Thermal Desalination Membranes. Adv. Funct. Mater. 29 (36).

Su, C.L., Horseman, T., Cao, H.B., Christie, K., Li, Y.P., Lin, S.H., 2019. Robust Superhydrophobic Membrane for Membrane Distillation with Excellent Scaling Resistance. Environ. Sci. Technol. 53 (20), 11801–11809.

Tao, P., Ni, G., Song, C., Shang, W., Wu, J., Zhu, J., Chen, G., Deng, T., 2018. Solar–driven interfacial evaporation. Nature Energy 3 (12), 1031–1041.

Tong, T., Elimelech, M., 2016. The global rise of zero liquid discharge for wastewater management: drivers, technologies, and future directions. Environ. Sci. Technol. 50 (13), 6846–6855.

Wang, Z.X., Horseman, T., Straub, A.P., Yip, N.Y., Li, D.Y., Elimelech, M., Lin, S.H., 2019a. Pathways and challenges for efficient solar-thermal desalination. Sci. Adv. 5 (7).

Wang, Q., Jia, F., Huang, A., Qin, Y., Song, S., Li, Y., Arroyo, M.A.C, 2020. MoS2@ sponge with double layer structure for high-efficiency solar desalination. Desalination 481, 114359.

Wang, M., Li, X., Hua, W.K., Shen, L.D., Yu, X.F., Wang, X.F., 2016. Electrospun Poly (acrylic acid)/Silica Hydrogel Nanofibers Scaffold for Highly Efficient Adsorption of Lanthanide Ions and Its Photoluminescence Performance. ACS Appl. Mater. Interfaces 8 (36), 23995–24007.

Wang, X.Y., Xue, J.Z., Ma, C.F., He, T., Qian, H.S., Wang, B., Liu, J.W., Lu, Y., 2019c. Anti-biofouling double-layered unidirectional scaffold for long-term solar-driven water evaporation. J. Mater. Chem. A 7 (28), 16696–16703.

Weng, D., Xu, F., Li, X., Li, Y., Sun, J., 2018. Bioinspired photothermal conversion coatings with self-healing superhydrophobicity for efficient solar steam generation. J. Mater. Chem. A 6 (47), 24441–24451.

Wang, S.F., Liu, M.S., Feng, Y., Bu, Y.R., Huynh, S.H., Ng, T.W., Gu, F., Yu, A.B., Jiang, X.C., 2017. Bioinspired hierarchical copper oxide surfaces for rapid dropwise condensation. J. Mater. Chem. A 5 (40), 21422–21428.

Wang, Y., Liu, H., Chen, C., Kuang, Y., Song, J., Xie, H., Jia, C., Kronthal, S., Xu, X., He, S., Hu, L., 2019b. All Natural, High Efficient Groundwater Extraction via Solar Steam/Vapor Generation. Adv. Sustain. Syst. 3 (1), 1800055.

Wei, C., Dai, F., Lin, L., An, Z., He, Y., Chen, X., Chen, L., Zhao, Y., 2018. Simplified and robust adhesive-free superhydrophobic SiO2-decorated PVDF membranes for efficient oil/water separation. J. Memb. Sci. 555, 220–228.

Wen, R., Xu, S., Ma, X., Lee, Y.C., Yang, R., 2018. Three-dimensional superhydrophobic nanowire networks for enhancing condensation heat transfer. Joule 2 (2), 269–279.

Wu, X., Chen, G.Y., Zhang, W., Liu, X., Xu, H., 2017. A Plant-Transpiration-Process-Inspired Strategy for Highly Efficient Solar Evaporation. Adv. Sustain. Syst. 1 (6), 1700046.

Wu, L., Dong, Z., Cai, Z., Ganapathy, T., Fang, N.X., Li, C., Yu, C., Zhang, Y., Song, Y., 2020. Highly efficient three-dimensional solar evaporator for high salinity desalination by localized crystallization. Nat. Commun. 11 (1), 1–12.

Wu, X., Robson, M.E., Phelps, J.L., Tan, J.S., Shao, B., Owens, G., Xu, H.L., 2019. A flexible photothermal cotton-CuS nanocage-agarose aerogel towards portable solar steam generation. Nano Energy 56, 708–715.

Xiao, P., He, J., Liang, Y., Zhang, C., Gu, J.C., Zhang, J.W., Huang, Y.J., Kuo, S.W., Chen, T., 2019a. Rationally Programmable Paper-Based Artificial Trees Toward Multipath Solar-Driven Water Extraction from Liquid/Solid Substrates. Solar Rrl 3 (7), 1900004.

Xiao, P., Gu, J., Zhang, C., Ni, F., Liang, Y., He, J., Zhang, L., Ouyang, J., Kuo, S.W., Chen, T., 2019b. A scalable, low-cost and robust photo-thermal fabric with tunable and programmable 2D/3D structures towards environmentally adaptable liquid/solid-medium water extraction. Nano Energy 65, 104002.

Xia, Y., Hou, Q., Jubaer, H., Li, Y., Kang, Y., Yuan, S., Liu, H., Woo, M.W., Zhang, L., Gao, L., 2019. Spatially isolating salt crystallisation from water evaporation for continuous solar steam generation and salt harvesting. Energy Environ. Sci..

Xu, N., Li, J., Wang, Y., Fang, C., Li, X., Wang, Y., Zhou, L., Zhu, B., Wu, Z., Zhu, S., Zhu, J., 2019a. A water lily-inspired hierarchical design for stable and efficient solar evaporation of high-salinity brine. Sci. Adv. 5 (7), eaaw7013.

Xu, W., Hu, X., Zhuang, S., Wang, Y., Li, X., Zhou, L., Zhu, S., Zhu, J., 2018. Flexible and salt resistant Janus absorbers by electrospinning for stable and efficient solar desalination. Adv. Energy Mater. 8 (14), 1702884.

Xu, Y., Liu, D., Xiang, H., Ren, S., Zhu, Z., Liu, D., Xu, H., Cui, F., Wang, W., 2019b. Easily scaled-up photo-thermal membrane with structure-dependent auto-cleaning feature for high-efficient solar desalination. J. Memb. Sci..

Yang, Y.W., Zhao, H.Y., Yin, Z.Y., Zhao, J.Q., Yin, X.T., Li, N., Yin, D.D., Li, Y.N., Lei, B., Du, Y.P., Que, W.X., 2018b. A general salt-resistant hydrophilic/hydrophobic nanoporous double layer design for efficient and stable solar water evaporation distillation. Mater. Horiz. 5 (6), 1143–1150.

Yang, Y., Li, X., Zheng, X., Chen, Z., Zhou, Q., Chen, Y., 2018a. 3D-Printed Biomimetic Super-Hydrophobic Structure for Microdroplet Manipulation and Oil/Water Separation. Adv. Mater. 30 (9), 1704912.

Yang, Y., Tong, Z., Ngai, T., Wang, C., 2014. Nitrogen-rich and fire-resistant carbon aerogels for the removal of oil contaminants from water. ACS Appl. Mater. Interfaces 6 (9), 6351–6360.

Zang, L.L., Bu, Z.P., Sun, L.G., Zhang, Y.H., 2016. Hollow carbon fiber sponges from crude catkins: an ultralow cost absorbent for oils and organic solvents. RSC Adv. 6 (54), 48715–48719.

Zang, L.L., Ma, J., Lv, D.W., Liu, Q.L., Jiao, W.L., Wang, P.P., 2017. A Core-shell Fiber-Constructed pH-responsive Nanofibrous Hydrogel Membrane for Efficient Oil/Water Separation. J. Mater. Chem. A 5 (36), 19398–19405.

Zeng, Y., Yao, J., Horri, B.A., Wang, K., Wu, Y., Li, D., Wang, H., 2011. Solar evaporation enhancement using floating light-absorbing magnetic particles. Energy Environ. Sci. 4 (10), 4074–4078.

Zeng, J., Wang, Q., Shi, Y., Liu, P., Chen, R., 2019b. Osmotic Pumping and Salt Rejection by Polyelectrolyte Hydrogel for Continuous Solar Desalination. Adv. Energy Mater., 1900552.

Zeng, J., Cui, S., Wang, Q., Chen, R., 2019a. Multi-layer temperature-responsive hydrogel for forward-osmosis desalination with high permeable flux and fast water release. Desalination 459, 105–113.

Zheng, Y., Gao, X., Jiang, L., 2007. Directional adhesion of superhydrophobic butterfly wings. Soft Matter 3 (2), 178–182.

Zhang, Q., Xiao, X.F., Wang, G., Ming, X., Liu, X.H., Wang, H., Yang, H.J., Xu, W.L., Wang, X.B., 2018. Silk-based Systems for Highly Efficient Photothermal Conversion under One Sun: portability, Flexibility, and Durability. J. Mater. Chem. A 6 (35), 17212–17219.

Zhang, C., Liang, H.Q., Xu, Z.K., Wang, Z., 2019a. Harnessing Solar-Driven Photothermal Effect toward the Water-Energy Nexus. Adv. Sci. 6 (18), 1900883.

Zhang, Q., Yang, H., Xiao, X., Wang, H., Yan, L., Shi, Z., Chen, Y., Xu, W., Wang, X., 2019b. A new self-desalting solar evaporation system based on a vertically oriented porous polyacrylonitrile foam. J. Mater. Chem. A 7 (24), 14620–14628.

Zhang, Q., Yi, G., Fu, Z., Yu, H., Chen, S., Quan, X., 2019c. Vertically Aligned Janus MXene-Based Aerogels for Solar Desalination with High Efficiency and Salt Resistance. ACS Nano 13 (11), 13196–13207.

Zhang, Q., Yi, G., Fu, Z., Yu, H., Chen, S., Quan, X., 2019d. Vertically Aligned Janus MXene-Based Aerogels for Solar Desalination with High Efficiency and Salt Resistance. ACS Nano.

Zhang, W., Zhang, G., Ji, Q., Liu, H., Liu, R., Qu, J., 2019e. Capillary-Flow-Optimized Heat Localization Induced by an Air-Enclosed Three-Dimensional Hierarchical Network for Elevated Solar Evaporation. ACS Appl. Mater. Interfaces 11 (10), 9974–9983.

Zha, X.-J., Zhao, X., Pu, J.-H., Tang, L.-S., Ke, K., Bao, R.-Y., Bai, L., Liu, Z.-Y., Yang, M.-B., Yang, W., 2019. Flexible anti-biofouling MXene/cellulose fibrous membrane for sustainable solar-driven water purification. ACS Appl. Mater. Interfaces 11 (40), 36589–36597.

Zhang, S., Zang, L., Dou, T., Zou, J., Zhang, Y., Sun, L., 2020. Willow Catkins-derived porous carbon membrane with hydrophilic property for efficient solar steam generation. ACS Omega 5 (6), 2878–2885.

Zhao, F., Zhou, X.Y., Shi, Y., Qian, X., Alexander, M., Zhao, X.P., Mendez, S., Yang, R.G., Qu, L.T., Yu, G.H., 2018a. Highly Efficient Solar Vapour Generation via Hierarchically Nanostructured Gels. Nat. Nanotechnol. 13 (6), 489–495.

Zhao, J., Yang, Y., Yang, C., Tian, Y., Han, Y., Liu, J., Yin, X., Que, W., 2018b. A hydrophobic surface enabled salt-blocking 2D Ti3C2 MXene membrane for efficient and stable solar desalination. J. Mater. Chem. A 6 (33), 16196–16204.

Zhao, F., Guo, Y., Zhou, X., Shi, W., Yu, G., 2020. Materials for solar-powered water evaporation. Nat. Rev. Mater. 5 (5), 388–401.

Zhou, X.Y., Zhao, F., Guo, Y.H., Zhang, Y., Yu, G.H., 2018. A Hydrogel-based Antifouling Solar Evaporator for Highly Efficient Water Desalination. Energy Environ. Sci. 11 (8), 1985–1992.

Zhou, X., Zhao, F., Guo, Y., Rosenberger, B., Yu, G., 2019a. Architecting Highly Hydratable Polymer Networks to Tune the Water State for Solar Water Purification. Sci. Adv. 5 (6), eaaw5484.

Zhou, X., Guo, Y., Zhao, F., Yu, G., 2019b. Hydrogels as an Emerging Material Platform for Solar Water Purification. Acc. Chem. Res. 52 (11), 3244–3253.

Zhu, M.W., Li, Y.J., Chen, G., Jiang, F., Yang, Z., Luo, X.G., Wang, Y.B., Lacey, S.D., Dai, J.Q., Wang, C.W., Jia, C., Wan, J.Y., Yao, Y.G., Gong, A., Yang, B., Yu, Z.F., Das, S., Hu, L.B., 2017. Tree-Inspired Design for High-Efficiency Water Extraction. Adv. Mater. 29 (44).

Zhu, M.W., Li, Y.J., Chen, F.J., Zhu, X.Y., Dai, J.Q., Li, Y.F., Yang, Z., Yan, X.J., Song, J.W., Wang, Y.B., Hitz, E., Luo, W., Lu, M.H., Yang, B., Hu, L.B., 2018. Plasmonic Wood for High-Efficiency Solar Steam Generation. Adv. Energy Mater. 8 (4).

Zhu, B., Kou, H., Liu, Z., Wang, Z., Macharia, D.K., Zhu, M., Wu, B., Liu, X., Chen, Z., 2019. Flexible and washable CNT-embedded PAN nonwoven fabrics for solar-enabled evaporation and desalination of seawater. ACS Appl. Mater. Interfaces 11 (38), 35005–35014.